Alleviating Defect and Oxidation in Tin Perovskite Solar Cells Using Bidentate Ligand

Dhruba B. Khadka[1]*, Yasuhiro Shirai[1]†, Masatoshi Yanagida[1], Terumasa Tadano[2], and Kenjiro Miyano[1]

[1] Photovoltaic Materials Group, Center for GREEN Research on Energy and Environmental Materials, National Institute for Materials Science (NIMS), 1-1 Namiki, Tsukuba, Ibaraki 305-0044, Japan

[2] Research Center for Magnetic and Spintronic Materials, National Institute for Materials Science (NIMS), 1-2-1 Sengen, Tsukuba, Ibaraki 305-0047, Japan.

Corresponding Author

*E-mail: KHADKA.B.Dhruba@nims.go.jp

ABSTRACT

Tin- perovskite solar cells (Sn-PSCs) have low energy conversion efficiency and stability due to facile oxidation of Sn^{2+} during precursor solution preparation and film growth. Herein, we introduced formohydrazide (FHZ) as a bidentate ligand into the Sn-halide perovskite (Sn-HaP) to improve the optoelectronic properties. This approach is found to be effective for the suppression of Sn-oxidation and interfacial energy band modulation. The depth profile distribution confirmed that the FHZ additive is primarily located on surfaces and HTL/Sn-HaP interface with partly capping at the grain boundaries which offers a reducing ambient in the Sn-HaP film. Therefore, the device with FHZ demonstrated the device efficiency of 12.87 % (9.93%- control) with enhanced open circuit voltage from ~0.734 to 0.874 V and improved operational device stability. The device analysis suggests that the FHZ additive alleviates the bulk and interface defect in the Sn-PSC with $-NH_2$ and -O=C bidentate bonding to Sn-HaP, which is supported by theoretical calculations. Thus, this work corroborates the importance of multidentate ligands for modulating the film morphology and defect chemistry in the Sn-perovskite for high efficiency and superior device stability.

1. Introduction

Lead halide perovskite solar cells (Pb-PSCs) have demonstrated outstanding improvement in power conversion efficiency (PCE) scaled over 25% in the past decade.[1] However, the potential risk of Pb in health and the environment has imposed a hurdle in commercialization. Therefore, lead-free perovskite candidates have centred colossal attention to solve the toxicity issue of lead.[2,3] Among the various alternative candidates, tin halide perovskite (Sn-HaP) derivatives are the most promising owing to their promising optoelectrical properties (such as small exciton binding energy, high carrier mobilities, and high absorption coefficients) with ideal bandgaps of 1.2- 1.4 eV.[4] However, there is a gap in device performance between Pb- and Sn-PSCs. It has been documented that the intrinsic instability due to the facile oxidation of Sn^{2+} to Sn^{4+} leads to an increase in Sn^{2+} vacancy density,[5] metal-like behavior,[6] and lower carrier diffusion length[7] in Sn-perovskite film.

Several reports have been documented on reducing Sn^{2+} oxidation,[8–14] surface passivation,[5,15,16] structural regulation,[17,18] and bulk[19] or interface engineering[20] for the improvement in PCE as well as device stability in the Sn-PSCs.[21] Template crystal growth with n-propylammonium iodide dripping has demonstrated the reconstruction of the intermediate phase into the preferred crystalline orientation.[7] A thin top 2D layer was formed on the 3D-HaP by post-treatment using such as phenethylammonium bromide (PEABr)/IPA[22] or 4-(trifluoromethyl)benzyl ammonium/chloroform.[23] Many reports have used multifunctional bulky hydrophobic cation derivatives[24–26] that form 3D/2D composite or hollow structures of Sn-perovskites resulting in promising device efficiency and stability. Similarly, the pseudohalide functional additives have been employed for defect passivation on the surface or bulk in Sn-perovskite.[15,27] Ning and co-workers have documented well-controlled crystal orientation using $SnI_2.(DMSO)_x$ adduct comprised with PEABr that scaled up its PCE.[28] Another competitive record result has been reported by modulating the 2D/3D microstructures of the Sn-HaP absorber layer using fluorine functionalized PEABr.[19] Moreover, the multidentate additives are also found to be effective for modulating Pb and Sn-perovskite film growth and defect chemistry.[29–33] Thus, functional additive engineering has been substantiated to be effective for the simultaneous realization of modulating the film microstructure and defect attenuation to obtain high-quality Sn-HaP films.

Here, we introduced formohydrazide (FHZ) as a bidentate ligand in the Sn-HaP precursor solution to attenuate the extent of tin oxidation and optoelectronic quality of Sn-perovskites. We achieved a significant leaping of PCE from 9.93 to 12.87 % with superior device stability. It is observed that the FHZ additive results in high-quality Sn-HaP film with highly oriented

crystalline growth, well-compact film texture, long carrier lifetime, and passivation of Sn^{2+} oxidation chemistry. DFT results suggest that the FHZ adsorbed on Sn-HaP with stronger bonding to Sn sites. The ToF-SIM analysis revealed that the FHZ additive is mainly distributed on the surface and grain boundaries or at the HTL/HaP interface of the 3D-Sn-HaPs resulting in effective defect passivation. This work underscores a detailed insight into a functional additive in Sn-PSCs with comprehensive characteristic insights coupled with the first-principles calculations.

2. Results and discussion

The Sn-HaP films were fabricated by spin-coating precursor solution with FHZ, bidentate ligand (-NH_2 and -O=C) as shown in Fig. 1a, b. It has been documented that multifunctional ligands coordinate synergistically with Pb^{2+} ions via strong chemical bonds.[31,34,35] It is aimed to improve the crystallization and passivating defect chemistry in the film by incorporating bidentate additive for the stronger bonding interaction to Sn-sites. As shown in Figure 1c, X-ray diffraction (XRD) patterns of Sn-HaP films with various mol% of FHZ additive are displayed (Fig. S1). XRD patterns display the characteristic diffraction assigned to highly oriented crystallographic planes of (100) and (200) which can be assigned to the orthorhombic phase of $FASnI_3$.[8,36] No additional peak in the small-angle regime (Fig. 1c, left) indicates the absence of 2D phase in Sn-HaP with FHZ additive. Although there is no shifting of characteristics XRD peak for the control or FHZ-added Sn-HaP films (Fig. 1c, right), the Sn-HaP film with FHZ additive showed comparatively intensified XRD characteristic peaks compared to the control film. This observation corroborates that the FHZ additive improved crystallinity, but it is not incorporated in the Sn-HaP crystal lattice. For further confirmation, we prepared Sn-HaP film by mixing 60 mol% of FHZ in the control precursor solution. The XRD pattern (Fig. S2) shows a similar crystal growth with an additional crystallographic plane of (102) and (122) of Sn-HaP indicating multi-orientation growth with higher FHZ content.

The absorption spectra of the films (Fig. S3) with varying FHZ contents are depicted in Fig. 1d. The spectral responses show a nuance effect at the band edge (inset in Fig.1d). The Sn-HaP with FHZ additive has rather steeper curve than the control film with slightly red shifting in bandgap (Fig. S4a). Moreover, Urbach energy estimated from absorption spectra (Fig. S4b) showed a lower value for the Sn-HaP film with FHZ additive (51 meV) compared to the control film (63 meV) suggesting suppression of defect at the band edge with the FHZ additive.[37]

Figure 1e displays the normalized photoluminescence (PL) spectra showing a slightly red shift of the characteristic peak at the band edge. The PL peaks are found to be centred at

1.430 ±0.02 eV for the control and 1.416 ±0.02 eV for 12 mol% FHZ (Fig. S4c). These values are parallel to the bandgap estimated from absorption spectra. Besides that, the PL spectra (Fig. S5) showed a higher peak intensity compared to the control Sn-HaP film indicating ameliorated film quality with the FHZ additive. The Sn-HaP with 12 mol% FHZ showed the highest PL characteristic peak intensity that is also consistent with the XRD peak intensity. Since the FHZ additive does not incorporate in the crystal lattice, the difference in absorption and PL characteristic spectra stems from the passivation at the interface or on surface defect rather than the lattice modification.[17,18]

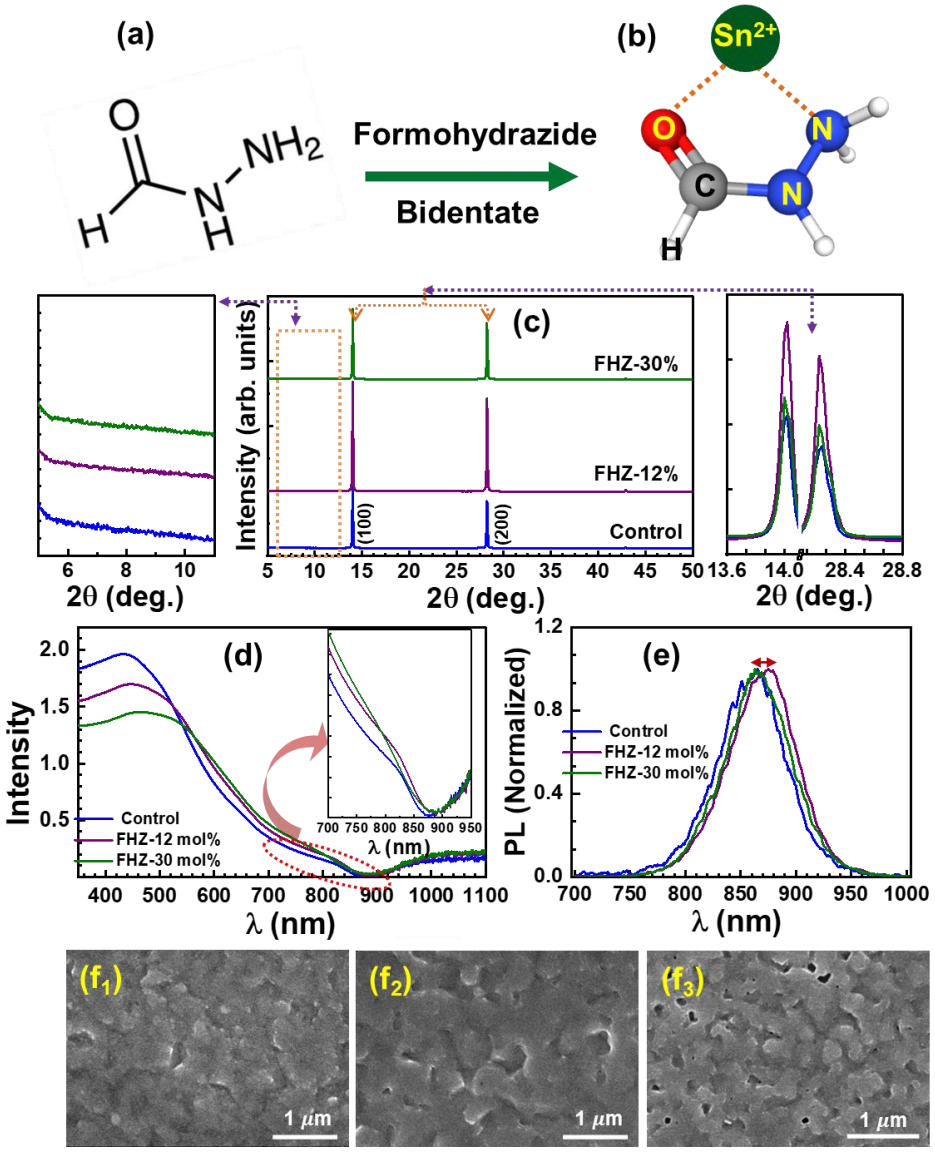

Figure 1. Molecular structure of bidentate additive (formohydrazide) (a) and bidentate ligand coordinating with Sn^{2+} (b). Growth characteristics of the $FASnI_3$ films with FHZ additive (0-30 mol%). (c) XRD results (left- 2θ<10: XRD patterns; right- magnified-XRD characteristics peaks [(100) and (200)]. (d) Absorption spectra (inset; magnified spectra at the band edge), (e)

PL spectra, and SEM images of Sn-HaP films; FHZ additives; 0 (control) (f_1), 12 mol% (f_2), and 30 mol% (f_3).

Scanning electron microscopic (SEM) images of the control and FHZ additive films are displayed in Fig. 1$f_{1\text{-}3}$ (Fig. S6). The films with FHZ additive exhibit comparatively compact and better film coverage by suppressing the pinhole's densities. Moreover, one can see small granular features in the top SEM image in the control film which disappeared in the FHZ-added film. However, the film with a higher FHZ additive (≥20 mol%) was found to grow with pinholes and uneven morphology (Fig. S2b, S6). It is learned that the rapid crystallization of Sn-HaP film forms pinhole-rich morphology that can be decelerated by functional additive engineering[38–43] and structural regulation.[17,18] It is shown that morphology can be tuned by dripping hot antisolvent or solvent vapor annealing with DMSO.[44] Some reports have documented the templated growth of Sn-HaP[7] and $SnI_2.(DMSO)_x$ complex[28] in Sn-HaP precursor for the improvement in film growth and optoelectronic quality. In the line of growth mechanism, it is believed that the FHZ additive with -NH_2 and -O=C extends the bonding interaction with SnI_2 which plays a crucial role to slow down the crystal growth and inhibit defect chemistry.[37,45] This facilitates the coarsening of grains and improves the Sn-HaP film quality.

To evaluate the effect of the FHZ additive on the photovoltaic performance, we fabricated Sn-PSC with the device layer structure as shown in Fig. 2a, b. It revealed that the Sn-PSC with FHZ additive grows with larger and wider columnar cross-sectional bulk that could facilitate carrier transport and attenuates the recombination densities in the device. The current density-voltage (*J-V*) characteristics with varying FHZ contents are given in Fig. S7 and the corresponding device parameters are summarized in Table S1. Figure 2c shows *J-V* curves of the control and the best Sn-PSCs with FHZ (12 mol%). The figures of merit are given in Table 1. The control device achieved an efficiency of 9.93% (with J_{SC} ~19.62 mA/cm^2, V_{OC} ~0.734 V, and FF ~69.01%). The device with FHZ additive (≤12 mol%) in Sn-HaP (hereafter, Sn-PSC with FHZ) improved the device PCE of ~12.87% with a significant increase in V_{OC} ~0.874 V and *FF* ~75.2% (steady-state J_{SC} and *PCE*; Fig. S8). This remarkable enhancement is attributed to the high crystalline quality, compact film morphology, and defect passivation, as will be discussed later. Our result is in the range of reported device performance as listed in Table S2 (supporting information). We observed a narrow distribution of device parameters (Figs. 2d and S9) for the Sn-PSCs with FHZ suggesting better reproducibility than the control device. Besides that, the Sn-PSCs with higher FHZ additive (>12 mol%) resulted in lower performance.

It is correlated to poor film morphology due to the deterioration of the Sn-HaP film surface and optophysical properties.

Figure 2e displays the external quantum efficiency (*EQE*) of Sn-PSCs. It shows almost similar spectra response except for slightly higher EQE at lower and higher wavelength regimes suggesting the slight improvement at the interface or band edge with FHZ additive.[46] The values of J_{SC} calculated from the *EQE* spectra are 19.31 and 19.24 mA/cm^2 for the device without and with FHZ additive, respectively. These results are parallel to the J_{SC} from the *J–V* results (Fig. 2c). It reveals a little red shifting for the device with FHZ of the band edge estimated form EQE spectra (Fig. S10). It is in close agreement with the bandgap calculated from the PL characteristic peak and absorption spectra (Fig. S4).

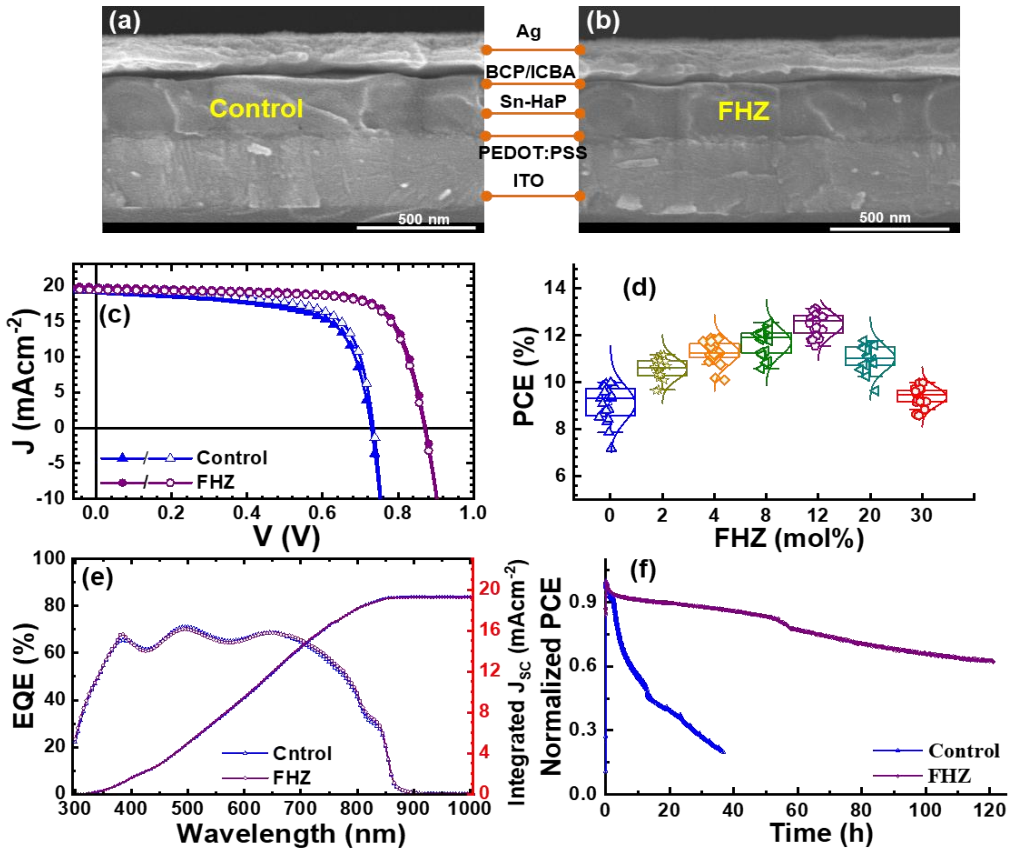

Figure 2. Cross-sectional SEM image of control (a) and FHZ additive (b) Sn-PSCs. *J-V* curves of devices (■ forward/□ reverse scan direction) (control and FHZ additive (12 mol%) (c), statistics of device efficiency (η) (d). *EQE* spectra (e). Operational stability of PSCs under MPPT conditions (f).

Table 1. Summarized device parameters of the Sn-PSCs without and with FHZ additive under one sun irradiation. The average PCE and standard deviation (SD) are obtained from 4 batches (20 devices).

Device	Scan direction	J_{SC} (mAcm^{-2})	V_{OC} (V)	*FF*	*PCE* (%)	PCE Average ± SD
Control	F	19.77	0.747	0.665	9.82	9.06 ± 0.73
	R	19.62	0.734	0.690	9.93	
FHZ	F	19.64	0.869	0.747	12.75	12.52 ± 0.47
	R	19.58	0.874	0.752	12.87	

We evaluated the long-term operational stability of the encapsulated control and FHZ additive devices under maximum power point tracking (MPPT) conditions. The device with FHZ additive demonstrated superior operational device stability as depicted in Fig. 2f. The control device's PCE dropped to <20% of initial PCE after 40 hours while the device with FHZ retained its PCE to ~62% of the original PCE after 120 hours. It corroborates that the Sn-HaP with FHZ is also propitious for the device's stability. Although this work demonstrates an improvement in device performance and stability, tin-based PSC is still far behind Pb-based PSC. Therefore, it still demands much effort to resolve the limitation factors for device parameters and operational stability.

To get insight into the enhancement in device performance, we investigated the characteristics of the control and FHZ devices. Figure 3a shows the light-intensity-dependent V_{OC} of the device that accounts for the charge recombination behavior in the device.[47] The control device estimates a slope of 1.59 k_BT/q which is higher than the device with FHZ additive (1.22 k_BT/q). It indicates a reduction in trap-assisted recombination in the FHZ device.[48]

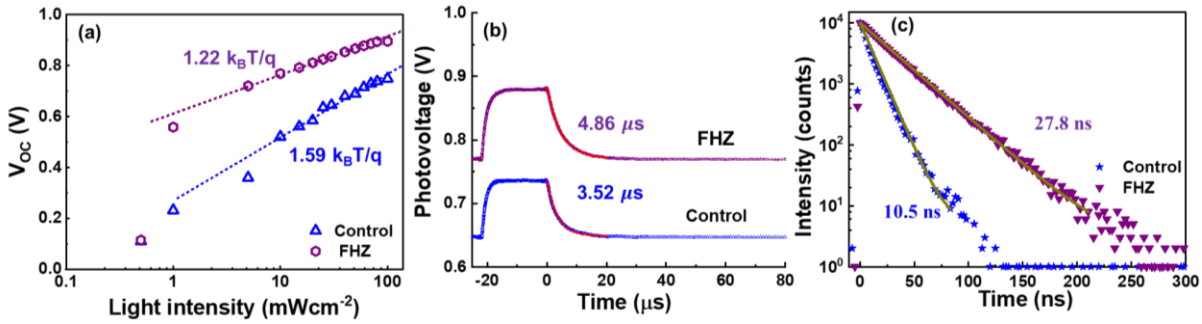

Figure 3. Light intensity dependence of V_{OC} (a) and TPV decay curves (b) of the control and FHZ additives Sn-PSCs. TRPL decay spectra for corresponding films (c).

We also evaluated the transient photovoltage (TPV) of respective devices depicted in Fig. 3b by modulating V_{OC} with transient illumination. The TPV decay curves demonstrated a longer carrier lifetime of 4.86 μs for the device with FHZ additive than that for the control

device (~3.52 μs), suggesting lower trap-assisted recombination. These characteristic results support the improvement in device performance with the FHZ additive. It is in line with other reports.[48,49]

To understand further carrier recombination, time-resolved photoluminescence (TRPL) responses (Figure 3c) were measured. The Sn-HaP film with FHZ demonstrates a longer carrier lifetime (τ_1~27.8 ns) compared to the control film (τ_1~10.5 ns). These results are in the range of other reports on Sn-HaP with functional additives.[36,38,50] It suggests that the recombination pathways have been suppressed in the Sn-HaP film with FHZ additive. It ameliorates the surface chemistry and quenches of recombination densities in the Sn-HaP bulk with bidentate ligand bonding with -NH_2 and -O=C bonding.[33,51]

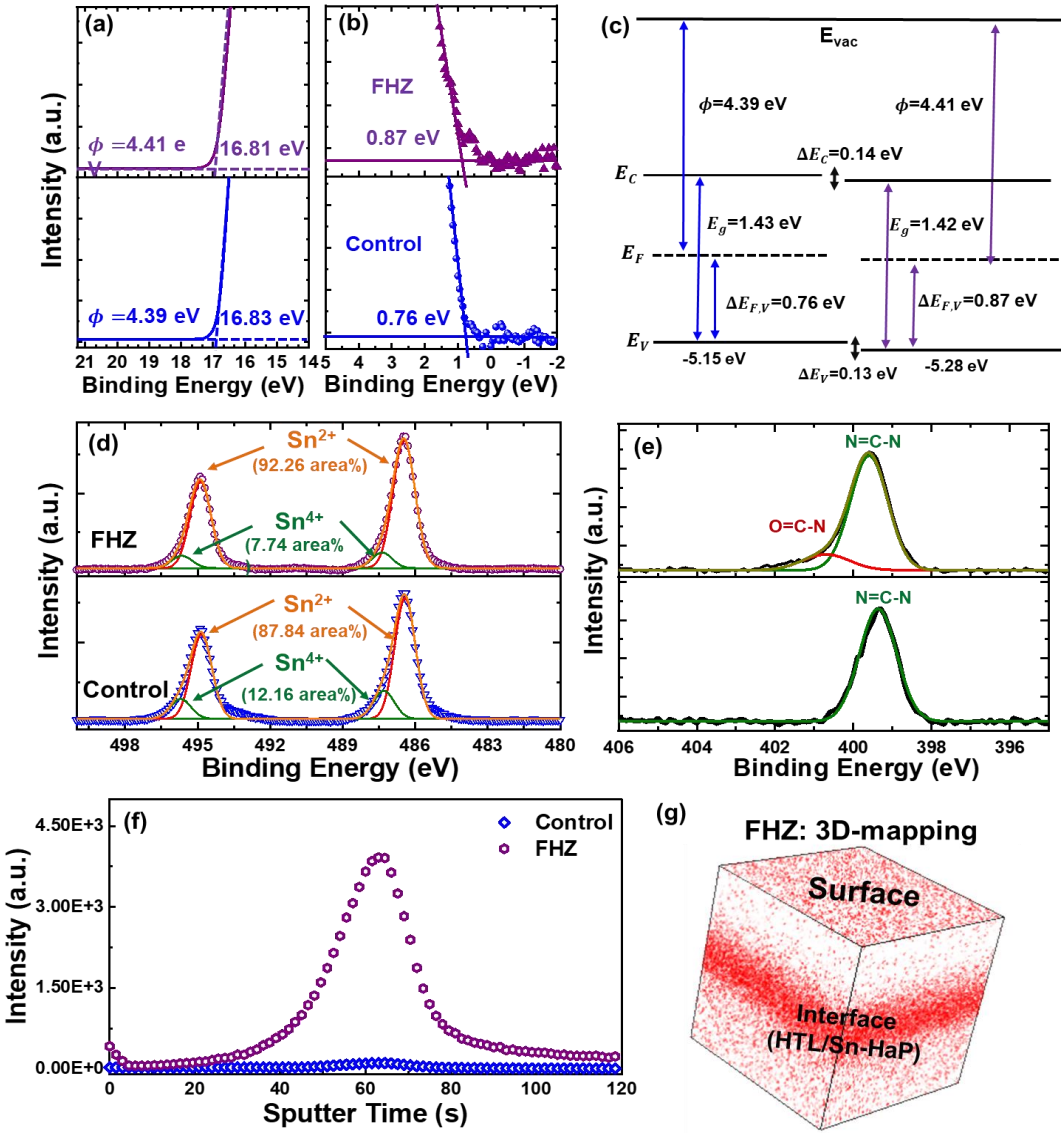

Figure 4. UPS spectra of the $FASnI_3$ films without and with FHZ; (a) the photoemission cutoff energy and (b) valence band spectra with the energy difference between the valence band maximum (E_V) and the Fermi level (E_F) and (c) schematic energy levels. XPS-spectra (d) Sn

3d: $3d_{5/2}$ and $3d_{3/2}$ and (e) N1s of the surface of the Sn-HaP films without and with FHZ. ToF-SIMS depth profile of Sn-HaP without and with FHZ additive for (f) CNO^- signal and (g) 3D image reconstructed from the ToF-SIM depth profile for FHZ (CNO^-).

To study the surface energy band, the control and FHZ-added films were characterized by ultraviolet photoelectron spectroscopy (UPS). It is found that the work function (ϕ) (Fig. 4a) and the difference between the valence band and Fermi level ($\Delta E_{F,V}$=E_V-E_F) (Fig. 4b) were slightly increased for the film with FHZ additive. The band structure (Fig. 4c, energy band diagram, Fig. S11) was constructed by accounting optical bandgap (Fig. S5). It shows that that the LUMO level offset of films (control and FHZ additive) with respect to ICBA changed from -0.02 and +0.08 eV while HOMO level offsets to the PEDOT: PSS are -0.1 and +0.03 eV. It demonstrates a down or upshift of E_C and E_V level and builds up a band offset with respect to PEDOT: PSS and C_{60} that could balance the carrier transport.[20,52] It is documented that a spike at the interfacial band is propitious for suppressing interfacial recombination.[53] It implicates that the energy band modulation of Sn-HaP with FHZ additive contributes for a slight increase in device parameters (especially $V_{OC,}$ FF) that partially supports for the enhancement in device performance.

Furthermore, the surface chemistry of respective films was investigated by X-ray photoelectron spectroscopy (XPS) (Fig. S12). To evaluate the oxidation of Sn, we analyzed the Sn characteristic peaks deconvoluted into the Sn 3d ($3d_{5/2}$ ($3d_{3/2}$)) (Fig. 4d) at ~486.7 (495.2) eV and 487.3 (495.7) eV which are attributed to the Sn^{2+} and Sn^{4+} species, respectively. It is found that the ionic percentage of Sn^{4+} in the Sn-HaP with FHZ additive is suppressed from 12.16 to 7.74%. The XPS spectra for Sn^{2+} shift towards higher binding energy for Sn-HaP film with FHZ additive indicating the stronger interaction SnI_2 and FHZ induced from bidentate coordination interaction (Sn^{2+}-NH_2 and Sn^{2+}-O=C bonding). The XPS spectra of C and N (Fig. 4e, Fig. S13) suggest that FHZ additive could introduce a stronger bonding strength against facile oxidation. FHZ, as a bidentate ligand can form a coordination complex with Sn^{2+} inhibiting oxidation on the surface and bulk of Sn-HaP film.[30,54] Hence, it ameliorates the defect chemistries of Sn-HaP film resulting in better film quality and hence device performance.

Moreover, the time-of-flight secondary ion mass spectrometry (ToF-SIMS) was carried out to confirm the distribution of Sn-HaP constituents and FHZ additive. The ToF-SIMS depth profiles (Fig. S14) show the key elements from the control and FHZ additive Sn-HaP films deposited on PEDOT:PSS/ITO substrates. Figure 4f (Fig. S14) revealed the signal CNO^- ion

from FHZ distributed throughout the Sn-HaP film with a higher concentration at the surface or interface of PEDOT:PSS/Sn-HaP. The 3D image (Fig. 4g) visualizes the FHZ (CNO^-) distribution. This result suggests that the FHZ distributes on the surface and at the interface which controls the extent of Sn oxidation in Sn-HaP as well as improves the HTL/Sn-HaP interface quality. It is also supported by other reports.[23,30] Indeed, the FHZ at the interface will ameliorate the interface quality by minimizing the corrosive effect of PEDOT:PSS to the Sn-perovskite bulk.[55,56] Therefore, it is suggested that the FHZ additive plays a role in ameliorating the material chemistry and attenuation of defect densities.

To explore the defect distribution, we investigate the capacitance characteristics of the Sn-PSCs and evaluate the effect of FHZ additive on the carrier profile, which also accounts for the carrier distribution (free carrier and defect density)[57–59] and ion or charge accumulation at the interface.[60] For the quantitative analysis of the carrier and defect profile, the Mott-Schottky (M-S) curves and carrier profile (Eqn.1) were calculated by the relation.[47]

$$N_{CV}=-\frac{2}{q\varepsilon_0\varepsilon_s}\left[\frac{d}{dV}\left(\frac{1}{C(V)^2}\right)\right]^{-1} \quad (1)$$

where C - capacitance per area, ε_0-permittivity of free space, ε_s - a dielectric constant of perovskite layer. N_{CV} represents the carrier distribution profile corresponding to calculated from C-V curves.

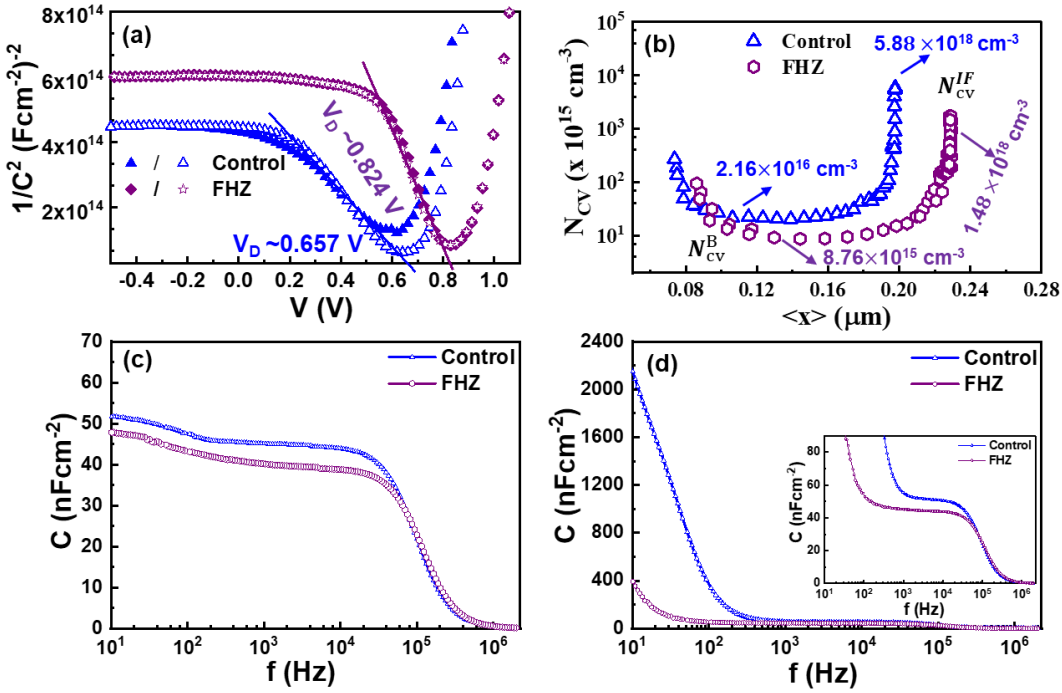

Figure 5. Capacitance analysis of devices; (a) M-S plots (symbol for scan direction; ■ forward/□ reverse). (b) Carrier profile calculated from C-V curves. C-f spectra (c, d) of devices under dark and illumination, respectively.

Figure 5a shows the *M-S* plots of respective devices with forward and reverse scan directions. One can see *M-S* curve hysteresis in the control device suggesting the lag of interfacial ionic motion or electric field induced by the charge accumulation at the interface. The diffusion potential (V_D)[47] is found to be increased from 0.657 V (the control) to 0.824 V (the device with FHZ). This is in line with a higher V_{OC} in the FHZ device. Figure 5b displays a U-shaped carrier distribution calculated from the C-V curves. The *C-V* analysis revealed that the bulk carrier density (N_{CV}^{B}) of ~2.16×10^{16} cm^{-3} in the control device was reduced by half (~8.76×10^{15} cm^{-3} for the device with FHZ additive). Similarly, the carrier profile at the edge which accounts for the interface defect profile is found to be decreased by approximately ~ one-fourth in the device with FHZ additive (N_{CV}^{IF} ~5.88×10^{18} for control to ~1.48×10^{18} cm^{-3} for the FHZ additive. It has been reported that the Sn-PSC with butylammonium iodide additive has improved device performance with a reduction in the carrier density (7.2×10^{16} cm^{-3} to 6.2×10^{16} cm^{-3}).[16] Similarly, the device with Br-doped $FASnI_3$ has been reported the carrier density attenuated by 3 orders (6.76×10^{17} to 7.80×10^{14} cm^{-3}).[61] It indicates that functional additives or compositional engineering play a vital role in defect passivation. The N_{CV} results consolidate that the FHZ additive mitigates the defect densities at the space charge region and interface. A lower N_{CV} profile for the device with FHZ is analogous to a longer carrier lifetime and the suppression of Sn^{2+} oxidation.

Figure 5c shows capacitance-frequency (*C-f*) spectra of Sn-PSCs. The control device has a slightly larger value in the range of 1kHz to 50 kHz that stems from the Sn-HaP layer indicating a higher defect density. It is reported that the C-f spectra at a lower frequency signifies ionic motion or charge accumulation.[60,62] The device with FHZ additive has a lower value indicating the suppressed ion or charge accumulation at the interfacial layer or electrode. Importantly, the C-f spectra under light (Fig. 5d) show a significantly higher capacitance at low frequencies compared to the high-frequency regime. It implies that the ion or carrier accumulation at the interface or electrode is significantly suppressed in the Sn-PSC with FHZ additive. It also explains the superior stability of the device with FHZ (Fig. 2f). Our work suggests that the functional ligand is advantageous for the improvement in the device performance and stability.

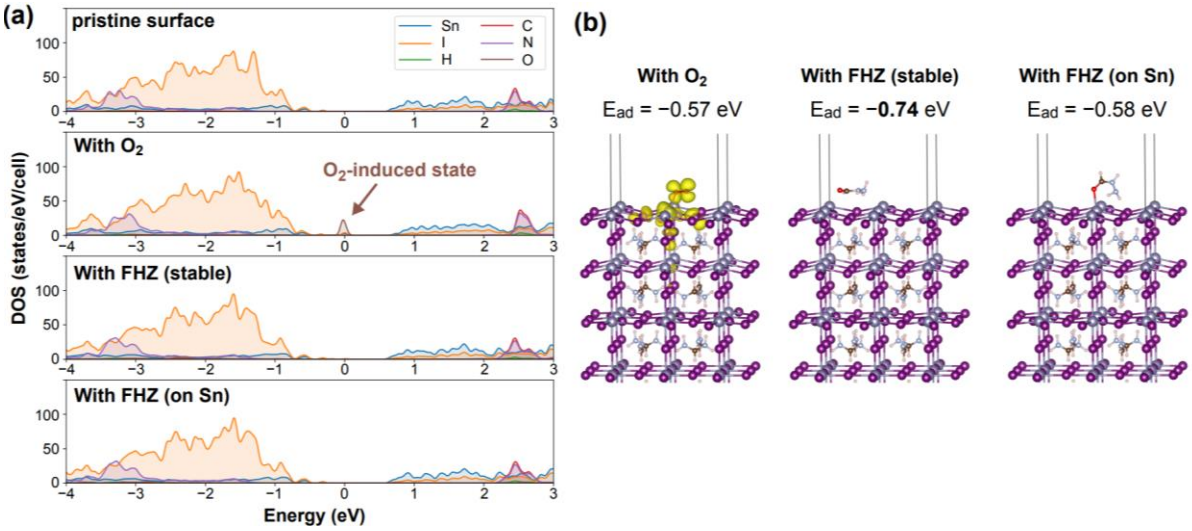

Figure 6. Adsorption energies and corresponding electronic density of states (DOS) computed for $FASnI_3$ with and without a molecule on the SnI_2-terminated surface. (a) Atom-projected DOS of the pristine SnI_2-terminated slab model of $FASnI_3$ and that with an O_2 or FHZ molecule on the surface. The energy is measured relative to the valence band maximum of the pristine case. (b) Stable adsorption patterns of O_2 or FHZ molecules on the SnI_2-terminated surface and the corresponding adsorption energies. For FHZ, adsorption selectively on an Sn atom is also shown for comparison. The figures were created with VESTA.[63]

Furthermore, we investigated the effect of the FHZ additive in Sn-HaP film by first-principles calculations based on density functional theory (DFT), where a slab model of a SnI_2-terminated surface was employed.[23,64] The computational details are described in the supporting information (experimental section and Fig. S15). Figure 6 shows DFT calculations results considering molecular interactions on the SnI_2-terminated surface of $FASnI_3$. An O_2 molecule is most stable when it is on top of an Sn atom, whose adsorption energy is $E_{\mathrm{ad}} = -0.57$ eV. However, this configuration induces an in-gap state (Fig. 6a) formed mainly by the oxygen *2p* state and the *5p* states of the Iodine atoms near the adsorption site. The charge density distribution is shown in Fig. 6b. By contrast, when an FHZ is added on the SnI_2-terminated surface, the molecule is found to be most stable when it is off the Sn site, as given in Fig. 6b. The corresponding adsorption energy is $E_{\mathrm{ad}} = -0.74$ eV, indicating that FHZ stays more strongly on the surface with -N and -O bidentate interaction. Moreover, the DOSs in Fig. 6a demonstrate that an FHZ does not induce any in-gap states which are deleterious to the photovoltaic performance. This trend is still observed even when an FHZ molecule is placed on top of Sn. These computational findings demonstrate the effectiveness of FHZ to passivate the $FASnI_3$ surface without forming any undesirable in-gap states. Hence, the theoretical

calculations explain the improvement in device performance and stability achieved experimentally.

3. Conclusions

We have achieved the Sn-PSC of efficiency ~12.87 % and improved stability using formohydrazide additive (9.93 % for the control device). The $FASnI_3$ with FHZ grows with a compact the film morphology and highly oriented crystallized film. It controlled the extent of Sn^{2+}/Sn^{4+} oxidation benefiting from the bidentate ligand. The $FASnI_3$ with FHZ enhances the carrier lifetime and modulate the band offset. ToF-SIMS results indicates that the FHZ additive is mainly situated at HTL/Sn-HaP interface and surface with partly capping at the grain boundaries. The capacitance analysis revealed that the device with FHZ has higher the diffusion potential (0.657 to 0.824 V) and attenuates the bulk or surface trap densities which is supported by theoretical calculations. These results suggest that the antioxidative functional additives could play a crucial role for inhibiting Sn^{2+} oxidation and defect passivation which improves the PCE and operational stability of Sn-PSCs.

4. Experimental Methods

4.1 Film and Device Fabrication Method and Characterizations

We prepared Sn-HaP precursor (0.85 mol) by dissolving a 9.2:0.8:10:1 stoichiometric ratio of FAI, RbCl, SnI_2, and SnF_2 adding EDAI-0.01 M and PEABr-0.05 M in dimethyl sulfoxide (DMSO) solvent. Sn-HaP films with FHZ additive were prepared by varying FHZ molar ratios with respect to SnI_2 content. The Sn-HaP films were deposited by spin-coating method using chlorobenzene as anti-solvent. The device was complicated with inverted device structure; ITO/PEDOT:PSS/Sn-HaP/ICBA/BCP/Ag. The fabrication details are given in Supporting Information.

We investigated the Sn-HaP films by measuring X-ray diffraction, scaning electron microscope (SEM), X-ray photoelectron spectroscopy, ultraviolet photoelectron spectroscopy, photoluminescence spectroscopy, fluorescence lifetime spectrometer, absorption spectroscopy, Time-of-flight secondary ion mass spectrometry.

Sn-PSC devices were characterized by measuring current density–voltage (J–V) curves, external quantum efficiency (EQE) spectra, transient photovoltage, and capacitance spectra.

The details of characterization conditions and instrumentation are mentioned in Supporting Information.

4.2 Theoretical Calculations

We conducted first principle electronic structure calculations based on density functional theory using the Vienna *ab initio* simulation package (VASP)[65] which iimpliments the projector-augmented wave (PAW) method.[66] A detailed of computational procedure is given in the supporting information.

ASSOCIATED CONTENT

Supporting Information

Supporting Information is available free of charge at the ACS website.

Experimental details, XRD patterns, Absorption spectra, PL spectra, SEM images, J-V data, Device statistics, XPS spectra, Energy band diagram, ToF-SIMS data, Device parameters table, Reported device data, Details of DFT calculation.

AUTHOR INFORMATION

Corresponding author.

*Email:KHADKA.B.Dhruba@nims.go.jp (D.B.K.)

ORCID

Dhruba B. Khadka: 0000-0001-9134-3890
Yasuhiro Shirai: 0000-0003-2164-5468
Masatoshi Yanagida: 0000-0002-8065-7875
Terumasa Tadano: 0000-0002-8132-2161
Kenjiro Miyano: 0000-0002-5869-3087

Notes

The authors declare no competing financial interest.

Acknowledgements

This work was supported by JST-Mirai Program Grant Number JPMJMI21E6, Japan. The authors are grateful to Dr. Hitoshi Ota, Yamaguchi Kazuo-San, and Nariaki Sato-San from NIMS battery research platform for the technical support during XRD, XPS and ToF-SIMS measurement and analysis.

Conflicts of interest

There are no conflicts to declare.

References

(1) Almora, O.; Baran, D.; Bazan, G. C.; Cabrera, C. I.; Erten-Ela, S.; Forberich, K.; Guo, F.; Hauch, J.; Ho-Baillie, A. W. Y.; Jacobsson, T. J.; Janssen, R. A. J.; Kirchartz, T.; Kopidakis, N.; Loi, M. A.; Lunt, R. R.; Mathew, X.; McGehee, M. D.; Min, J.; Mitzi, D. B.; Nazeeruddin, M. K.; Nelson, J.; Nogueira, A. F.; Paetzold, U. W.; Rand, B. P.; Rau, U.; Snaith, H. J.; Unger, E.; Vaillant-Roca, L.; Yang, C.; Yip, H.; Brabec, C. J. Device Performance of Emerging Photovoltaic Materials (Version 3). *Adv. Energy Mater.* **2023**, *13* (1), 2203313. https://doi.org/10.1002/aenm.202203313.

(2) Pandian, M. G. M.; Khadka, D. B.; Shirai, Y.; Umedov, S.; Yanagida, M.; Subashchandran, S.; Grigorieva, A.; Miyano, K. Effect of Solvent Vapour Annealing on Bismuth Triiodide Film for Photovoltaic Applications and Its Optoelectronic Properties. *J. Mater. Chem. C* **2020**, *8* (35), 12173–12180. https://doi.org/10.1039/D0TC02455D.

(3) Nasti, G.; Abate, A. Tin Halide Perovskite (ASnX3) Solar Cells: A Comprehensive Guide toward the Highest Power Conversion Efficiency. *Adv. Energy Mater.* **2020**, *10* (13), 1902467. https://doi.org/10.1002/aenm.201902467.

(4) Baranowski, M.; Plochocka, P. Excitons in Metal-Halide Perovskites. *Adv. Energy Mater.* **2020**, *10* (26), 1903659. https://doi.org/10.1002/aenm.201903659.

(5) Kamarudin, M. A.; Hirotani, D.; Wang, Z.; Hamada, K.; Nishimura, K.; Shen, Q.; Toyoda, T.; Iikubo, S.; Minemoto, T.; Yoshino, K.; Hayase, S. Suppression of Charge Carrier Recombination in Lead-Free Tin Halide Perovskite via Lewis Base Post-Treatment. *J. Phys. Chem. Lett.* **2019**, *10* (17), 5277–5283. https://doi.org/10.1021/acs.jpclett.9b02024.

(6) Hao, F.; Stoumpos, C. C.; Guo, P.; Zhou, N.; Marks, T. J.; Chang, R. P. H.; Kanatzidis, M. G. Solvent-Mediated Crystallization of CH3NH3SnI3 Films for Heterojunction Depleted Perovskite Solar Cells. *J. Am. Chem. Soc.* **2015**, *137* (35), 11445–11452. https://doi.org/10.1021/jacs.5b06658.

(7) Liu, X.; Wu, T.; Chen, J.-Y.; Meng, X.; He, X.; Noda, T.; Chen, H.; Yang, X.; Segawa, H.; Wang, Y.; Han, L. Templated Growth of FASnI 3 Crystals for Efficient Tin Perovskite Solar Cells. *Energy Environ. Sci.* **2020**, *13* (9), 2896–2902. https://doi.org/10.1039/D0EE01845G.

(8) Liao, W.; Zhao, D.; Yu, Y.; Grice, C. R.; Wang, C.; Cimaroli, A. J.; Schulz, P.; Meng,

W.; Zhu, K.; Xiong, R.-G.; Yan, Y. Lead-Free Inverted Planar Formamidinium Tin Triiodide Perovskite Solar Cells Achieving Power Conversion Efficiencies up to 6.22%. *Adv. Mater.* **2016**, *28* (42), 9333–9340. https://doi.org/10.1002/adma.201602992.

(9) Lin, R.; Xiao, K.; Qin, Z.; Han, Q.; Zhang, C.; Wei, M.; Saidaminov, M. I.; Gao, Y.; Xu, J.; Xiao, M.; Li, A.; Zhu, J.; Sargent, E. H.; Tan, H. Monolithic All-Perovskite Tandem Solar Cells with 24.8% Efficiency Exploiting Comproportionation to Suppress Sn(Ii) Oxidation in Precursor Ink. *Nat. Energy* **2019**, *4* (10), 864–873. https://doi.org/10.1038/s41560-019-0466-3.

(10) Tsarev, S.; Boldyreva, A. G.; Luchkin, S. Y.; Elshobaki, M.; Afanasov, M. I.; Stevenson, K. J.; Troshin, P. A. Hydrazinium-Assisted Stabilisation of Methylammonium Tin Iodide for Lead-Free Perovskite Solar Cells. *J. Mater. Chem. A* **2018**, *6* (43), 21389–21395. https://doi.org/10.1039/C8TA07699E.

(11) Wang, C.; Zhang, Y.; Gu, F.; Zhao, Z.; Li, H.; Jiang, H.; Bian, Z.; Liu, Z. Illumination Durability and High-Efficiency Sn-Based Perovskite Solar Cell under Coordinated Control of Phenylhydrazine and Halogen Ions. *Matter* **2021**, *4* (2), 709–721. https://doi.org/10.1016/j.matt.2020.11.012.

(12) Li, B.; Di, H.; Chang, B.; Yin, R.; Fu, L.; Zhang, Y.-N.; Yin, L. Efficient Passivation Strategy on Sn Related Defects for High Performance All-Inorganic CsSnI3 Perovskite Solar Cells. *Adv. Funct. Mater.* **2021**, *31* (11), 2007447. https://doi.org/https://doi.org/10.1002/adfm.202007447.

(13) Lee, S. J.; Shin, S. S.; Kim, Y. C.; Kim, D.; Ahn, T. K.; Noh, J. H.; Seo, J.; Seok, S. Il. Fabrication of Efficient Formamidinium Tin Iodide Perovskite Solar Cells through SnF 2 -Pyrazine Complex. *J. Am. Chem. Soc.* **2016**, *138* (12), 3974–3977. https://doi.org/10.1021/jacs.6b00142.

(14) Nakamura, T.; Yakumaru, S.; Truong, M. A.; Kim, K.; Liu, J.; Hu, S.; Otsuka, K.; Hashimoto, R.; Murdey, R.; Sasamori, T.; Kim, H. Do; Ohkita, H.; Handa, T.; Kanemitsu, Y.; Wakamiya, A. Sn(IV)-Free Tin Perovskite Films Realized by in Situ Sn(0) Nanoparticle Treatment of the Precursor Solution. *Nat. Commun.* **2020**, *11* (1), 3008. https://doi.org/10.1038/s41467-020-16726-3.

(15) Jokar, E.; Chuang, H.-S.; Kuan, C.-H.; Wu, H.-P.; Hou, C.-H.; Shyue, J.-J.; Wei-Guang Diau, E. Slow Passivation and Inverted Hysteresis for Hybrid Tin Perovskite Solar Cells

Attaining 13.5% via Sequential Deposition. *J. Phys. Chem. Lett.* **2021**, 10106–10111. https://doi.org/10.1021/acs.jpclett.1c03107.

(16) Jokar, E.; Chien, C.-H.; Fathi, A.; Rameez, M.; Chang, Y.-H.; Diau, E. W.-G. Slow Surface Passivation and Crystal Relaxation with Additives to Improve Device Performance and Durability for Tin-Based Perovskite Solar Cells. *Energy Environ. Sci.* **2018**, *11* (9), 2353–2362. https://doi.org/10.1039/C8EE00956B.

(17) Khadka, D. B.; Shirai, Y.; Yanagida, M.; Miyano, K. Attenuating the Defect Activities with a Rubidium Additive for Efficient and Stable Sn-Based Halide Perovskite Solar Cells. *J. Mater. Chem. C* **2020**, *8* (7), 2307–2313. https://doi.org/10.1039/C9TC06206H.

(18) Gao, W.; Ran, C.; Li, J.; Dong, H.; Jiao, B.; Zhang, L.; Lan, X.; Hou, X.; Wu, Z. Robust Stability of Efficient Lead-Free Formamidinium Tin Iodide Perovskite Solar Cells Realized by Structural Regulation. *J. Phys. Chem. Lett.* **2018**, *9* (24), 6999–7006. https://doi.org/10.1021/acs.jpclett.8b03194.

(19) Yu, B.; Chen, Z.; Zhu, Y.; Wang, Y.; Han, B.; Chen, G.; Zhang, X.; Du, Z.; He, Z. Heterogeneous 2D/3D Tin-Halides Perovskite Solar Cells with Certified Conversion Efficiency Breaking 14%. *Adv. Mater.* **2021**, *33* (36), 2102055. https://doi.org/10.1002/adma.202102055.

(20) Jiang, X.; Wang, F.; Wei, Q.; Li, H.; Shang, Y.; Zhou, W.; Wang, C.; Cheng, P.; Chen, Q.; Chen, L.; Ning, Z. Ultra-High Open-Circuit Voltage of Tin Perovskite Solar Cells via an Electron Transporting Layer Design. *Nat. Commun.* **2020**, *11* (1), 1245. https://doi.org/10.1038/s41467-020-15078-2.

(21) Yan, Y.; Pullerits, T.; Zheng, K.; Liang, Z. Advancing Tin Halide Perovskites: Strategies toward the ASnX3 Paradigm for Efficient and Durable Optoelectronics. *ACS Energy Lett.* **2020**, *5* (6), 2052–2086. https://doi.org/10.1021/acsenergylett.0c00577.

(22) Liao, M.; Yu, B.-B.; Jin, Z.; Chen, W.; Zhu, Y.; Zhang, X.; Yao, W.; Duan, T.; Djerdj, I.; He, Z. Efficient and Stable FASnI3 Perovskite Solar Cells with Effective Interface Modulation by Low-Dimensional Perovskite Layer. *ChemSusChem* **2019**, *12* (22), 5007–5014. https://doi.org/10.1002/cssc.201902000.

(23) Wu, T.; Cui, D.; Liu, X.; Meng, X.; Wang, Y.; Noda, T.; Segawa, H.; Yang, X.; Zhang, Y.; Han, L. Efficient and Stable Tin Perovskite Solar Cells Enabled by Graded

Heterostructure of Light-Absorbing Layer. *Sol. RRL* **2020**, *4* (9), 2000240. https://doi.org/10.1002/solr.202000240.

(24) Ke, W.; Stoumpos, C. C.; Zhu, M.; Mao, L.; Spanopoulos, I.; Liu, J.; Kontsevoi, O. Y.; Chen, M.; Sarma, D.; Zhang, Y.; Wasielewski, M. R.; Kanatzidis, M. G. Enhanced Photovoltaic Performance and Stability with a New Type of Hollow 3D Perovskite {en}FASnI 3. *Sci. Adv.* **2017**, *3* (8). https://doi.org/10.1126/sciadv.1701293.

(25) Nishimura, K.; Kamarudin, M. A.; Hirotani, D.; Hamada, K.; Shen, Q.; Iikubo, S.; Minemoto, T.; Yoshino, K.; Hayase, S. Lead-Free Tin-Halide Perovskite Solar Cells with 13% Efficiency. *Nano Energy* **2020**, *74*, 104858. https://doi.org/10.1016/j.nanoen.2020.104858.

(26) Jokar, E.; Cheng, P.-Y.; Lin, C.-Y.; Narra, S.; Shahbazi, S.; Wei-Guang Diau, E. Enhanced Performance and Stability of 3D/2D Tin Perovskite Solar Cells Fabricated with a Sequential Solution Deposition. *ACS Energy Lett.* **2021**, *6* (2), 485–492. https://doi.org/10.1021/acsenergylett.0c02305.

(27) Khadka, D. B.; Shirai, Y.; Yanagida, M.; Miyano, K. Pseudohalide Functional Additives in Tin Halide Perovskite for Efficient and Stable Pb-Free Perovskite Solar Cells. *ACS Appl. Energy Mater.* **2021**, *4* (11), 12819–12826. https://doi.org/10.1021/acsaem.1c02496.

(28) Jiang, X.; Li, H.; Zhou, Q.; Wei, Q.; Wei, M.; Jiang, L.; Wang, Z.; Peng, Z.; Wang, F.; Zang, Z.; Xu, K.; Hou, Y.; Teale, S.; Zhou, W.; Si, R.; Gao, X.; Sargent, E. H.; Ning, Z. One-Step Synthesis of SnI2·(DMSO)x Adducts for High-Performance Tin Perovskite Solar Cells. *J. Am. Chem. Soc.* **2021**, *143* (29), 10970–10976. https://doi.org/10.1021/jacs.1c03032.

(29) Chen, J.; Kim, S.-G.; Ren, X.; Jung, H. S.; Park, N.-G. Effect of Bidentate and Tridentate Additives on the Photovoltaic Performance and Stability of Perovskite Solar Cells. *J. Mater. Chem. A* **2019**, *7* (9), 4977–4987. https://doi.org/10.1039/C8TA11977E.

(30) Lin, Z.; Liu, C.; Liu, G.; Yang, J.; Duan, X.; Tan, L.; Chen, Y. Preparation of Efficient Inverted Tin-Based Perovskite Solar Cells via the Bidentate Coordination Effect of 8-Hydroxyquinoline. *Chem. Commun.* **2020**, *56* (28), 4007–4010. https://doi.org/10.1039/D0CC01106A.

(31) Che, Y.; Liu, Z.; Duan, Y.; Wang, J.; Yang, S.; Xu, D.; Xiang, W.; Wang, T.; Yuan, N.; Ding, J.; Liu, S. (Frank). Hydrazide Derivatives for Defect Passivation in Pure CsPbI3 Perovskite Solar Cells. *Angew. Chemie Int. Ed.* **2022**, *61* (33), e202205012. https://doi.org/10.1002/anie.202205012.

(32) Zhao, W.; Xu, J.; He, K.; Cai, Y.; Han, Y.; Yang, S.; Zhan, S.; Wang, D.; Liu, Z.; Liu, S. A Special Additive Enables All Cations and Anions Passivation for Stable Perovskite Solar Cells with Efficiency over 23%. *Nano-Micro Lett.* **2021**, *13* (1), 169. https://doi.org/10.1007/s40820-021-00688-2.

(33) Wang, J.; Che, Y.; Duan, Y.; Liu, Z.; Yang, S.; Xu, D.; Fang, Z.; Lei, X.; Li, Y.; Liu, S. (Frank). 21.15%-Efficiency and Stable Γ-CsPbI 3 Perovskite Solar Cells Enabled by an Acyloin Ligand. *Adv. Mater.* **2023**, 2210223. https://doi.org/10.1002/adma.202210223.

(34) Wang, X.; Ran, X.; Liu, X.; Gu, H.; Zuo, S.; Hui, W.; Lu, H.; Sun, B.; Gao, X.; Zhang, J.; Xia, Y.; Chen, Y.; Huang, W. Tailoring Component Interaction for Air-Processed Efficient and Stable All-Inorganic Perovskite Photovoltaic. *Angew. Chemie Int. Ed.* **2020**, *59* (32), 13354–13361. https://doi.org/10.1002/anie.202004256.

(35) Fu, S.; Wang, J.; Liu, X.; Yuan, H.; Xu, Z.; Long, Y.; Zhang, J.; Huang, L.; Hu, Z.; Zhu, Y. Multifunctional Liquid Additive Strategy for Highly Efficient and Stable CsPbI2Br All-Inorganic Perovskite Solar Cells. *Chem. Eng. J.* **2021**, *422*, 130572. https://doi.org/10.1016/j.cej.2021.130572.

(36) Wang, C.; Gu, F.; Zhao, Z.; Rao, H.; Qiu, Y.; Cai, Z.; Zhan, G.; Li, X.; Sun, B.; Yu, X.; Zhao, B.; Liu, Z.; Bian, Z.; Huang, C. Self-Repairing Tin-Based Perovskite Solar Cells with a Breakthrough Efficiency Over 11%. *Adv. Mater.* **2020**, *32* (31), 1907623. https://doi.org/10.1002/adma.201907623.

(37) Meng, X.; Lin, J.; Liu, X.; He, X.; Wang, Y.; Noda, T.; Wu, T.; Yang, X.; Han, L. Highly Stable and Efficient FASnI 3 -Based Perovskite Solar Cells by Introducing Hydrogen Bonding. *Adv. Mater.* **2019**, *31* (42), 1903721. https://doi.org/10.1002/adma.201903721.

(38) Jokar, E.; Chien, C.-H.; Tsai, C.-M.; Fathi, A.; Diau, E. W.-G. Robust Tin-Based Perovskite Solar Cells with Hybrid Organic Cations to Attain Efficiency Approaching 10%. *Adv. Mater.* **2019**, *31* (2), 1804835. https://doi.org/10.1002/adma.201804835.

(39) Shao, S.; Liu, J.; Portale, G.; Fang, H.-H.; Blake, G. R.; ten Brink, G. H.; Koster, L. J.

A.; Loi, M. A. Highly Reproducible Sn-Based Hybrid Perovskite Solar Cells with 9% Efficiency. *Adv. Energy Mater.* **2018**, *8* (4), 1702019. https://doi.org/10.1002/aenm.201702019.

(40) Jeong, J.; Kim, M.; Seo, J.; Lu, H.; Ahlawat, P.; Mishra, A.; Yang, Y.; Hope, M. A.; Eickemeyer, F. T.; Kim, M.; Yoon, Y. J.; Choi, I. W.; Darwich, B. P.; Choi, S. J.; Jo, Y.; Lee, J. H.; Walker, B.; Zakeeruddin, S. M.; Emsley, L.; Rothlisberger, U.; Hagfeldt, A.; Kim, D. S.; Grätzel, M.; Kim, J. Y. Pseudo-Halide Anion Engineering for α-FAPbI3 Perovskite Solar Cells. *Nature* **2021**, *592* (7854), 381–385. https://doi.org/10.1038/s41586-021-03406-5.

(41) Tong, J.; Song, Z.; Kim, D. H.; Chen, X.; Chen, C.; Palmstrom, A. F.; Ndione, P. F.; Reese, M. O.; Dunfield, S. P.; Reid, O. G.; Liu, J.; Zhang, F.; Harvey, S. P.; Li, Z.; Christensen, S. T.; Teeter, G.; Zhao, D.; Al-Jassim, M. M.; van Hest, M. F. A. M.; Beard, M. C.; Shaheen, S. E.; Berry, J. J.; Yan, Y.; Zhu, K. Carrier Lifetimes of >1 Ms in Sn-Pb Perovskites Enable Efficient All-Perovskite Tandem Solar Cells. *Science* **2019**, *364* (6439), 475–479. https://doi.org/10.1126/science.aav7911.

(42) Rameez, M.; Lin, E. Y.-R.; Raghunath, P.; Narra, S.; Song, D.; Lin, M.-C.; Hung, C.-H.; Diau, E. W.-G. Development of Hybrid Pseudohalide Tin Perovskites for Highly Stable Carbon-Electrode Solar Cells. *ACS Appl. Mater. Interfaces* **2020**, *12* (19), 21739–21747. https://doi.org/10.1021/acsami.0c03704.

(43) Yu, B.; Shi, J.; Tan, S.; Cui, Y.; Zhao, W.; Wu, H.; Luo, Y.; Li, D.; Meng, Q. Efficient (>20%) and Stable All-Inorganic Cesium Lead Triiodide Solar Cell Enabled by Thiocyanate Molten Salts. *Angew. Chemie Int. Ed.* **2021**, *60* (24), 13436–13443. https://doi.org/10.1002/anie.202102466.

(44) Liu, J.; Ozaki, M.; Yakumaru, S.; Handa, T.; Nishikubo, R.; Kanemitsu, Y.; Saeki, A.; Murata, Y.; Murdey, R.; Wakamiya, A. Lead-Free Solar Cells Based on Tin Halide Perovskite Films with High Coverage and Improved Aggregation. *Angew. Chemie Int. Ed.* **2018**, *57* (40), 13221–13225. https://doi.org/10.1002/anie.201808385.

(45) Zheng, C.; Qiu, P.; Zhong, S.; Luo, X.; Wu, S.; Wang, Q.; Gao, J.; Lu, X.; Gao, X.; Shui, L.; Wu, S.; Liu, J. Dual Effects of Slow Recrystallization and Defects Passivation Achieve Efficient Tin-Based Perovskite Solar Cells with Good Stability Up to One Year. *Adv. Funct. Mater.* **2023**, 2212106. https://doi.org/10.1002/adfm.202212106.

(46) Nakane, A.; Tampo, H.; Tamakoshi, M.; Fujimoto, S.; Kim, K. M.; Kim, S.; Shibata, H.; Niki, S.; Fujiwara, H. Quantitative Determination of Optical and Recombination Losses in Thin-Film Photovoltaic Devices Based on External Quantum Efficiency Analysis. *J. Appl. Phys.* **2016**, *120* (6), 064505. https://doi.org/10.1063/1.4960698.

(47) Khadka, D. B.; Shirai, Y.; Yanagida, M.; Masuda, T.; Miyano, K. Enhancement in Efficiency and Optoelectronic Quality of Perovskite Thin Films Annealed in MACl Vapor. *Sustain. Energy Fuels* **2017**, *1* (4), 755–766. https://doi.org/10.1039/C7SE00033B.

(48) Zhu, J.; Park, S.; Gong, O. Y.; Sohn, C.; Li, Z.; Zhang, Z.; Jo, B.; Kim, W.; Han, G. S.; Kim, D. H.; Ahn, T. K.; Lee, J.; Jung, H. S. Formamidine Disulfide Oxidant as a Localised Electron Scavenger for >20% Perovskite Solar Cell Modules. *Energy Environ. Sci.* **2021**, *14* (9), 4903–4914. https://doi.org/10.1039/D1EE01440D.

(49) Yang, S.; Chen, S.; Mosconi, E.; Fang, Y.; Xiao, X.; Wang, C.; Zhou, Y.; Yu, Z.; Zhao, J.; Gao, Y.; De Angelis, F.; Huang, J. Stabilizing Halide Perovskite Surfaces for Solar Cell Operation with Wide-Bandgap Lead Oxysalts. *Science* **2019**, *365* (6452), 473 LP – 478. https://doi.org/10.1126/science.aax3294.

(50) Zhu, Z.; Mi, Q. Substituted Thiourea as Versatile Ligands for Crystallization Control and Surface Passivation of Tin-Based Perovskite. *Cell Reports Phys. Sci.* **2022**, *3* (1), 100690. https://doi.org/10.1016/j.xcrp.2021.100690.

(51) Hu, M.; Wang, G.; Zhang, Q.; Gong, J.; Xing, Z.; Gao, J.; Wang, J.; Zeng, P.; Zheng, S.; Liu, M.; Zhou, Y.; Yang, S. Antioxidative Solution Processing Yields Exceptional Sn(II) Stability for Sub-1.4 EV Bandgap Inorganic Perovskite Solar Cells. *J. Energy Chem.* **2022**, *72*, 487–494. https://doi.org/10.1016/j.jechem.2022.05.030.

(52) Li, B.; Wu, X.; Zhang, H.; Zhang, S.; Li, Z.; Gao, D.; Zhang, C.; Chen, M.; Xiao, S.; Jen, A. K. -Y.; Yang, S.; Zhu, Z. Efficient and Stable Tin Perovskite Solar Cells by Pyridine-Functionalized Fullerene with Reduced Interfacial Energy Loss. *Adv. Funct. Mater.* **2022**, *32* (39), 2205870. https://doi.org/10.1002/adfm.202205870.

(53) Ding, C.; Zhang, Y.; Liu, F.; Kitabatake, Y.; Hayase, S.; Toyoda, T.; Yoshino, K.; Minemoto, T.; Katayama, K.; Shen, Q. Effect of the Conduction Band Offset on Interfacial Recombination Behavior of the Planar Perovskite Solar Cells. *Nano Energy* **2018**, *53*, 17–26. https://doi.org/10.1016/j.nanoen.2018.08.031.

(54) Sanchez-Diaz, J.; Sánchez, R. S.; Masi, S.; Krecmarová, M.; Alvarez, A. O.; Barea, E. M.; Rodriguez-Romero, J.; Chirvony, V. S.; Sánchez-Royo, J. F.; Martinez-Pastor, J. P.; Mora-Seró, I. Tin Perovskite Solar Cells with;1,300 h of Operational Stability in N2 through a Synergistic Chemical Engineering Approach. *Joule* **2022**, *6* (4), 861–883. https://doi.org/10.1016/j.joule.2022.02.014.

(55) Wang, Q.; Chueh, C. C.; Eslamian, M.; Jen, A. K. Y. Modulation of PEDOT:PSS PH for Efficient Inverted Perovskite Solar Cells with Reduced Potential Loss and Enhanced Stability. *ACS Appl. Mater. Interfaces* **2016**, *8* (46), 32068–32076. https://doi.org/10.1021/acsami.6b11757.

(56) Cameron, J.; Skabara, P. J. The Damaging Effects of the Acidity in PEDOT:PSS on Semiconductor Device Performance and Solutions Based on Non-Acidic Alternatives. *Mater. Horizons* **2020**, *7* (7), 1759–1772. https://doi.org/10.1039/C9MH01978B.

(57) Khadka, D. B.; Shirai, Y.; Yanagida, M.; Miyano, K. Insights into Accelerated Degradation of Perovskite Solar Cells under Continuous Illumination Driven by Thermal Stress and Interfacial Junction. *ACS Appl. Energy Mater.* **2021**, *4* (10), 11121–11132. https://doi.org/10.1021/acsaem.1c02037.

(58) Khadka, D. B.; Shirai, Y.; Yanagida, M.; Miyano, K. Unraveling the Impacts Induced by Organic and Inorganic Hole Transport Layers in Inverted Halide Perovskite Solar Cells. *ACS Appl. Mater. Interfaces* **2019**, *11* (7), 7055–7065. https://doi.org/10.1021/acsami.8b20924.

(59) Warren, C. W.; Roe, E. T.; Miller, D. W.; Shafarman, W. N.; Lonergan, M. C. An Improved Method for Determining Carrier Densities via Drive Level Capacitance Profiling. *Appl. Phys. Lett.* **2017**, *110* (20), 203901. https://doi.org/10.1063/1.4983367.

(60) Miyano, K.; Yanagida, M.; Shirai, Y. Impedance Spectroscopy Revisited. *Adv. Energy Mater.* **2020**, *10* (26), 1903097. https://doi.org/10.1002/aenm.201903097.

(61) Lee, S. J.; Shin, S. S.; Im, J.; Ahn, T. K.; Noh, J. H.; Jeon, N. J.; Seok, S. Il; Seo, J. Reducing Carrier Density in Formamidinium Tin Perovskites and Its Beneficial Effects on Stability and Efficiency of Perovskite Solar Cells. *ACS Energy Lett.* **2018**, *3* (1), 46–53. https://doi.org/10.1021/acsenergylett.7b00976.

(62) Eames, C.; Frost, J. M.; Barnes, P. R. F.; O'Regan, B. C.; Walsh, A.; Islam, M. S. Ionic

Transport in Hybrid Lead Iodide Perovskite Solar Cells. *Nat. Commun.* **2015**, *6* (1), 7497. https://doi.org/10.1038/ncomms8497.

(63) Momma, K.; Izumi, F. VESTA 3 for Three-Dimensional Visualization of Crystal, Volumetric and Morphology Data. *J. Appl. Crystallogr.* **2011**, *44* (6), 1272–1276. https://doi.org/10.1107/S0021889811038970.

(64) Khadka, D. B.; Shirai, Y.; Yanagida, M.; Tadano, T.; Miyano, K. Interfacial Embedding for High-Efficiency and Stable Methylammonium-Free Perovskite Solar Cells with Fluoroarene Hydrazine. *Adv. Energy Mater.* **2022**, *12* (38), 2202029. https://doi.org/10.1002/aenm.202202029.

(65) Kresse, G.; Furthmüller, J. Efficient Iterative Schemes for Ab Initio Total-Energy Calculations Using a Plane-Wave Basis Set. *Phys. Rev. B* **1996**, *54* (16), 11169–11186. https://doi.org/10.1103/PhysRevB.54.11169.

(66) Kresse, G.; Joubert, D. From Ultrasoft Pseudopotentials to the Projector Augmented-Wave Method. *Phys. Rev. B* **1999**, *59* (3), 1758–1775. https://doi.org/10.1103/PhysRevB.59.1758.

Table of content graphics

The formohydrazide, bidentate ligand in Sn-perovskite film enhanced the device efficiency to 12.87% with superior stability. This improvement is as a consequence of the reduction of the extent of Sn^{2+} oxidation, reconstruction of the interface, and passivation of the defect in the Sn-HaP film.